Environmental Science & Technology

pubs.acs.org/est

Article

Efficient Electroreduction of Low Nitrate Concentration via Nitrate Self-Enrichment and Active Hydrogen Inducement on the Ce(IV)-Co_3O_4 Cathode

Changhui Zhou, Yan Zhang, Chaoyue Xie, Jing Bai,* Jinhua Li, Haichuan Zhang, Hong Zhu, Mingce Long, Baoxue Zhou,* and Gengfeng Zheng*

Cite This: *Environ. Sci. Technol.* 2024, 58, 14940−14948

Read Online

ACCESS | Metrics & More | Article Recommendations | Supporting Information

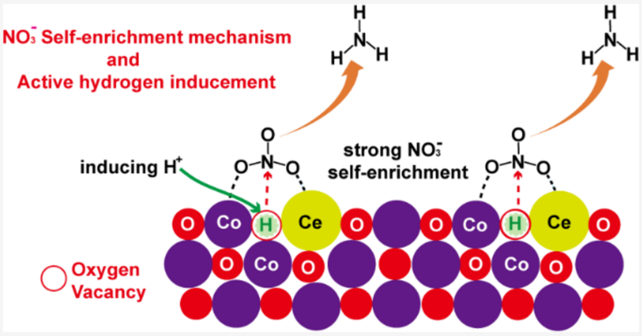

ABSTRACT: Low concentrations of nitrate (NO_3^-) widely exist in wastewater, post-treated wastewater, and natural environments; its further disposal is a challenge but meaningful for its discharge goals. Electroreduction of NO_3^- is a promising method that allows to eliminate NO_3^- and even generate higher-value NH_3. However, the massive side reaction of hydrogen evolution has raised great obstacles in the electroreduction of low concentrations of NO_3^-. Herein, we present an efficient electroreduction method for low or even ultralow concentrations of NO_3^- via NO_3^- self-enrichment and active hydrogen (H*) inducement on the Ce(IV)-Co_3O_4 cathode. The key mechanism is that the strong oxytropism of Ce(IV) in Co_3O_4 resulted in two changes in structures, including loose nanoporous structures with copious dual adsorption sites of Ce−Co showing strong self-enrichment of NO_3^- and abundant oxygen vacancies (O_{vs}) inducing substantial H*. Ultimately, the bifunctional role synergistically promoted the selective conversion of NH_3 rather than H_2. As a result, Ce(IV)-Co_3O_4 demonstrated a NO_3^- self-enrichment with a 4.3-fold up-adsorption, a 7.5-fold enhancement of NH_3 Faradic efficiency, and a 93.1% diminution of energy consumption when compared to Co_3O_4, substantially exceeding other reported electroreduction cathodes for NO_3^- concentrations lower than 100 mg·L^{-1}. This work provides an effective treatment method for low or even ultralow concentrations of NO_3^-.

KEYWORDS: *self-enrichment, active hydrogen, Ce(IV)-Co_3O_4, low nitrate concentrations, electroreduction*

■ INTRODUCTION

The natural nitrogen cycle is significantly affected by human activities, especially the wide distribution of nitrate (NO_3^-) in water bodies,[1−3] which is the main cause of photochemical smog, methemoglobinemia, and cancer.[4−6] Hence, further disposal of NO_3^- from water is becoming progressively critical. On the other hand, ammonia (NH_3) is not only an ideal, zero-carbon energy carrier in sustainable energy systems but also an essential feedstock for industrial production.[7−9] Researchers have been investigating new NH_3 synthetic approaches under mild reaction conditions to overcome the large energy consumption and carbon emission issues of the Haber−Bosch process.[10−13] Among various ammonia synthesis technologies, the electrochemical NO_3^- reduction reaction (NO_3RR), powered by renewable energy sources, uses electrons as a reducing agent with high efficiency and greenness that allows to simultaneously eliminate NO_3^- and generate NH_3.[14−19]

The reports about the electroreduction NO_3^- to NH_3 has significantly increased over the last 5 years with the catalyst designs focusing on the NH_3 yield,[20] NH_3 selectivity,[21] and current density.[22] Nonetheless, most of those reported studies pay close attention to relatively concentrated NO_3^- (>100 mM or 1400 mg·L^{-1} NO_3^--N),[23−28] which are beneficial for efficient reactant mass transfer near the catalyst−electrolyte interface[29] and inhibition of the hydrogen evolution reaction (HER) side reaction.[24,30] However, the electrochemical reduction of high concentrations of NO_3^- faces the problem of decrease in NO_3^- concentration, of which these water with diluted NO_3^- still cannot meet the discharge requirements.[31,32] Hence, substantial energy is required to concentrate the low concentrations of NO_3^- around the cathodic surface for further treatment,[33] greatly affecting the practical application. For instance, palladium (Pd) has previously been demonstrated with the capability of electro-reducing NO_3^- to NH_3, while at

Received: June 21, 2024
Revised: July 30, 2024
Accepted: July 30, 2024
Published: August 6, 2024

https://doi.org/10.1021/acs.est.4c06263
Environ. Sci. Technol. 2024, 58, 14940−14948

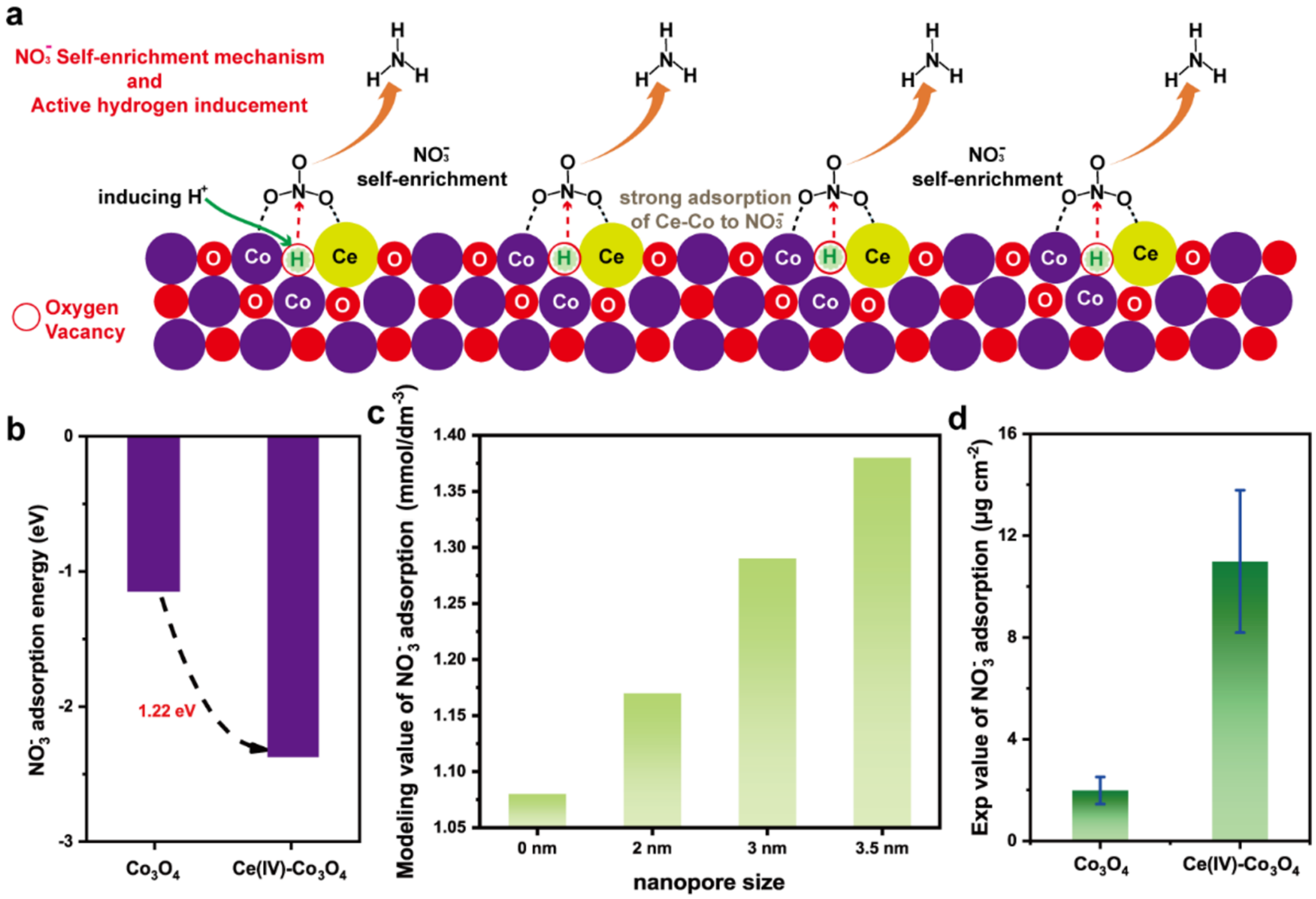

Figure 1. (a) Schematic mechanism of the self-enrichment and active hydrogen proliferation via Ce(IV)-Co_3O_4. (b) Calculated NO_3^- adsorption energies at the Co−Co dual site of Co_3O_4 and the Ce−Co dual site of Ce(IV)-Co_3O_4. (c) Simulated concentrations and distributions of local NO_3^- on the Ce(IV)-Co_3O_4 nanosheet surface for different pore size structures at 5 μs. The value of 3.5 nm was the maximum pore size of the constructed model, and the maximum concentration value from the simulation results was taken as the local NO_3^- concentration. (d) Actual adsorption of Co_3O_4 and Ce(IV)-Co_3O_4 at 1 mM·NO_3^-.

low NO_3^- concentrations (<100 mg·L^{-1} NO_3^--N),[29] the Faradic efficiency (FE) and partial current density of producing NH_3 remain limited due to the poor adsorption of NO_3^- on Pd.[34,35] Moreover, the typical abundancy of NO_3^- concentrations in common wastewater, post-treated wastewater, or natural environments is low, e.g., seven ∼50 mg·L^{-1} (0.5−3.5 mM, Table S1). Even about 80% of industrial or agricultural polluted runoff has concentration of less than 10 mg·L^{-1} (ultralow concentrations),[36,37] which still needs to be further reduced to meet the standard limit (Table S2). Thus, to achieve a reduction of low NO_3^- concentrations, it is necessary to address the enrichment and effective conversion around the electrode surface simultaneously.

Herein, we demonstrated the incorporation of CeO_2 and Co_3O_4 to form a CeO_2/Co_3O_4 nanocomposite (designated Ce(IV)-Co_3O_4) for the electroreduction of low concentrations of NO_3^- to NH_3 (Figure 1a). The strong oxytropism of Ce(IV) in Co_3O_4 resulted in two changes of loose nanoporous structures and abundant oxygen vacancies (O_{vs}) in structures since the large radius of Ce distorted the lattice of Co_3O_4, weakened the bond of Co−O, and engraved oxygen defect simultaneously. The positively charged dual sites of Ce−Co in loose nanoporous structures exhibited strong attraction to NO_3^-, realizing a higher enrichment for NO_3^-. The negatively charged centers of the O_{vs} activated H^+ to realize the proliferation of active hydrogen (H*). Ultimately, the bifunctional role between the NO_3^- self-enrichment and utilization of proliferative H* makes it possible to selectively synthesize NH_3 ranther than H_2 in low or even ultralow concentrations of NO_3^-. As results, Ce(IV)-Co_3O_4 exhibited superb performance over a wide NO_3^- concentration range (10−1000 mg·L^{-1} NO_3^--N); especially, it showed an excellent FE for nitrate reduction activity (NRA) of 92.3% and a low energy consumption (149.4 kWh/kg-N) in 10 mg·L^{-1} NO_3^- solution, substantially exceeding those of pristine Co_3O_4 or Pd, and represented the highest reported data at low NO_3^- concentrations (<100 mg·L^{-1} NO_3^--N). Hence, this work provides an effective method for the treatment of the NO_3^- water body, including high, low, or even ultralow concentrations.

MATERIALS AND METHODS

Chemicals. All chemicals were purchased from Sinopharm Chemical Reagent Co. Ltd. Deionized water was produced from a Millipore Milli-Q grade, with a resistivity of 18.2 MΩ·cm, and used for all experiments.

Synthesis of the Ce(IV)-Co_3O_4/Copper Foam. The Ce(IV)-Co_3O_4/copper foam was prepared via the reported method with a slight modification.[38] Prior to electrodeposition, copper foam (CF) was successively washed with ethanol and dilute hydrochloric acid. The first was synthesized on the CF by electrodeposition from a solution of the corresponding metal nitrate(s) with a total concentration of 0.1 M. The synthesis of the Ce-doped $Co(OH)_2$ precursor was as follows: 10 mol percent (mol %) of $Co(NO_3)_2$ in the solution was replaced with $Ce(NO_3)_3$, Ag/AgCl was the reference electrode, Pt mesh was the counter electrode, and a constant potential of −1.0 V vs Ag/AgCl was applied on the substrates for 10 min. After electrodeposition, the Ce-doped $Co(OH)_2$ precursors were placed inside a tube furnace and then heated at 400 °C for 2 h under a N_2 atmosphere. The obtained products were denoted as Ce(IV)-Co_3O_4/CF, of which the model structure of Ce(IV)-Co_3O_4 is provided in Figure S1. For the synthesis of different percentages of Ce in Co_3O_4/CF, different percents of Ce in Co_3O_4/CF were obtained with the same method, but different mol percents (mol %) of $Co(NO_3)_2$ in the solution were replaced with $Ce(NO_3)_3$.

Synthesis of Co_3O_4/CF and CeO_2/CF. The synthesis of the $Co(OH)_2$ and $Ce(OH)_3$ precursors was performed according to the synthesis of Ce(IV)-Co_3O_4/CF; solutions with only 0.1 M $Co(NO_3)_2$ solution and 0.1 M $Ce(NO_3)_3$ solution were used. After electrodeposition, the precursors were placed inside a furnace and then heated to 400 °C for 2 h. The obtained products were denoted as Co_3O_4/CF and CeO_2/CF.

Other detailed methods are provided in the Supporting Information.

RESULTS AND DISCUSSION

Catalyst Characterization. Ce(IV)-Co_3O_4 was prepared by the in situ electrodeposition of Ce−$Co(OH)_2$, followed by thermal annealing. X-ray diffraction (XRD) was applied to detect the crystalline structures of Ce(IV)-Co_3O_4. Figure S2a shows that the obvious diffraction peaks were mainly attributed to Co_3O_4 signals, and a CoO peak clearly appeared on Co_3O_4 and Ce(IV)-Co_3O_4.[38,39] In addition, the tiny diffraction of CeO_2 (∼28.5°) was observed in the XRD owing to the low Ce content in the sample.[38] Figure S2b displays the results of Fourier transform infrared (FTIR) spectroscopy. In addition to the evident peak at ∼566 and 644 cm^{-1} corresponding to the Co−O bond on Ce(IV)-Co_3O_4 and Co_3O_4,[40] the Ce−O stretching vibration located at ∼1060 cm^{-1} was attributed to the formation of CeO_2 on Co_3O_4,[41] suggesting that the successful introduction of CeO_2 into Co_3O_4.

Scanning electron microscopy (SEM) images showed that Ce(IV)-Co_3O_4 nanosheets with petal shapes were homogeneously deposited on the copper foam surface. The average nanosheet sizes were ∼200 nm (Figure S3), with abundant loose nanopores on the nanosheets (Figure S4). Atomic force microscopy (AFM) study showed that the thickness of Ce(IV)-Co_3O_4 was determined to be ∼3.6 nm (Figure S5a). Transmission electron microscopy (TEM) images showed the lamellar structure of Ce(IV)-Co_3O_4 (Figure S5b). Energy-dispersive X-ray spectroscopy (EDS) elemental mappings confirmed the uniform distributions of Co, Ce, and O elements across the whole sample, in which the atomic ratio of Ce and Co was ∼1:10 (Figure S5c). High-resolution TEM (HRTEM) images showed visible lattice spacings of 0.240, 0.286, and 0.310 nm (Figure S 5d), corresponding to the CoO (200), Co_3O_4 (220), and CeO_2 (111) planes.[39] These results confirmed that CeO_2 was successfully introduced into Co_3O_4. Many interfacial vacancies were observed on the CeO_2 and Co_3O_4 interface (Figure S5e).

Additionally, X-ray photoelectron spectroscopy (XPS) was conducted to investigate the chemical status of Co and O (Figure S6). The high-resolution O 1s and Co 2p spectra of Co_3O_4 and Ce(IV)-Co_3O_4 are shown in Figure S7a,b. The presence of Co^{2+} and Co^{3+} was observed on both Co_3O_4 and Ce(IV)-Co_3O_4 and deconvoluted into four peaks.[42] Ce(IV)-Co_3O_4 contained a higher Co^{2+}/Co^{3+} ratio (∼45/55) than Co_3O_4 (∼30/70), suggesting the higher content of Co^{2+} and the existence of a fraction of oxygen vacancies (O_{vs}).[39,43] As shown in Figure S7b, the oxygen species of the surface hydroxyl groups (−OH), lattice oxygen (O_L), and O_{vs} were present on the surface of the catalyst.[44] Ce(IV)-Co_3O_4 exhibited a much higher O_v fraction (48%) than Co_3O_4 (11%), which was potentially due to the stronger interaction between Ce and O in Ce(IV)-Co_3O_4.[45] The Raman spectra of Co_3O_4 and Ce(IV)-Co_3O_4 are displayed in Figure S7c. The characteristic Raman peaks were located at approximately 680, 516, and 475 cm^{-1}, corresponding to the typical Raman-active modes of A_{1g}, F_{2g}, and E_{2g}.[46] Note that the A_{1g} peak of Ce(IV)-Co_3O_4 shifted to a higher frequency than that of Co_3O_4, which signified the change in the long-range order of the crystal, indicating the formation of the O_{vs}. Furthermore, Ce(IV)-Co_3O_4 showed a stronger signal (g = 2.006) of electron paramagnetic resonance (EPR) compared with Co_3O_4 (Figure S7d). This result was associated with the vacancy center and further confirmed the amplification of O_{vs} in Ce(IV)-Co_3O_4.[47] Thus, introducing Ce atoms could regulate the microstructure and improve the Co^{2+} content by weakening the bond of Co and O to induce loose nanoporous structure and amplify O_{vs}.

Theoretical Analysis. To get an understanding of NO_3RR via Ce(IV)-Co_3O_4, the structure−activity relationship was investigated. At low NO_3^- concentration, the competitive adsorption of H_2O leads to the occurrence of H−H dimerization, resulting in the production of H_2 and a decrease of the Faradic efficiency (FE) for NO_3RR.[48] Hence, the better NO_3^- enrichment on the catalyst could obviously inhibit the H−H dimerization. First, the density functional theory (DFT) calculations were applied to conduct the NO_3^- and H_2O adsorption free energies on the Ce and Co sites. In Figure S8a, Ce(IV)-Co_3O_4 required −0.97 eV of H_2O adsorption energy, which is much more positive than the NO_3^- adsorption energy (−2.37 eV) with the gap of 1.40 eV, while the gap of adsorption energy between H_2O and NO_3^- on Co_3O_4 was 0.81 eV (Figure S8b), which indicated that introducing Ce ions into Co_3O_4 can suppress the negative impact of H_2O. Figure 1b shows the adsorption energies of NO_3^- on the Co−Co dual site and the Ce−Co dual site in Co_3O_4 and Ce(IV)-Co_3O_4, respectively. Notably, Ce(IV) had an extremely strong affinity for oxygen of NO_3^-, in which the Ce−Co dual site (−2.37 eV) showed a more negative adsorption energy than the Co−Co dual site (−1.05 eV), meaning the preferential NO_3^- adsorption on the Ce(IV)-Co_3O_4 catalyst. Comparing the adsorption energy of NO_3^- on other sites of Ce(IV)-Co_3O_4 (Figure S9), it was found that the Ce−Co dual site indeed exhibited the best adsorption capacity.

On the other hand, COMSOL Multiphysics was utilized to simulate the electric field distribution around the surface under different morphologies (Figure S10). A denser electric field distribution in the electrode region indicated that the geometry of the loose nanopores greatly increased the specific capacity, thus expanding the NO_3^- reduction.[49] Subsequently, finite element method (FEM) analysis was applied to simultaneously simulate the local concentration of NO_3^- around Co_3O_4 and

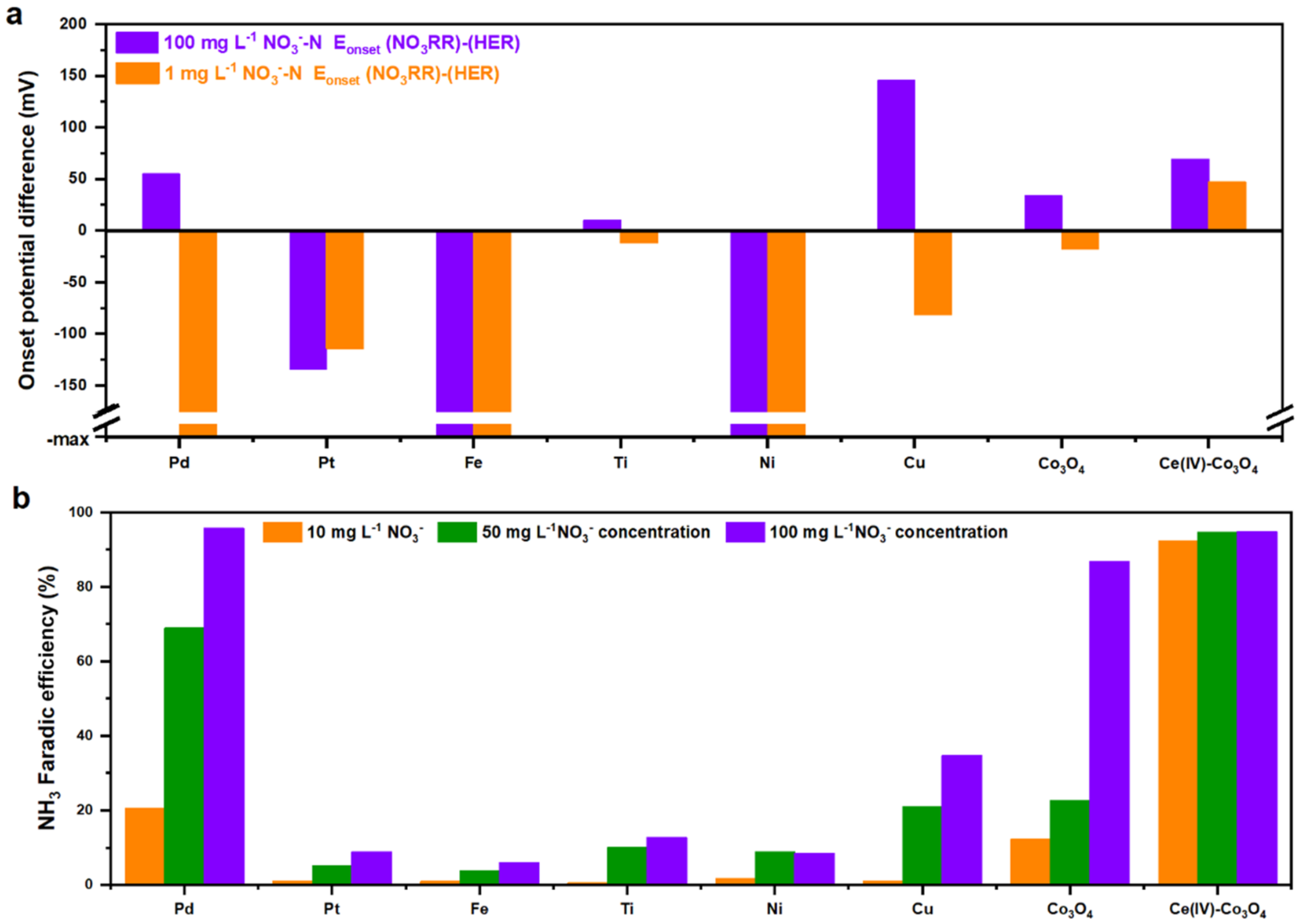

Figure 2. Catalysts with a distinctive electrocatalytic preference between the NO_3^- reduction reaction (NO_3RR) and hydrogen evolution reaction (HER). (a) Onset potential difference between the NO_3^- reduction reaction and HER: "$E_{onset}(NO_3RR) - E_{onset}(HER)$". −max means only HER proceed. LSV curves of the different catalysts in three different solutions: 0.1 M Na_2SO_4 (black curve) and 0.1 M Na_2SO_4 with 1−100 mg·L^{-1} NO_3^-. A scan rate of 10 mV·s^{-1} was used for LSV on all catalysts. The geometric area of catalyst was 1 cm^2. (b) NH_3 Faradic efficiency difference between NO_3^- electroreduction to NH_3. The FEs obtained by converting the half concentration of NO_3^- to NH_3 for comparison.

Ce(IV)-Co_3O_4. With the diffusion, more NO_3^- accumulated on the surface of Ce(IV)-Co_3O_4 (Figure S11a), while little NO_3^- migrated to the surface of Co_3O_4 (Figure S11b) owing to the self-enrichment of Ce(IV)-Co_3O_4. As the simulated results show in Figure 1c, in nanoporous structure, the enrichment increases with the expansion of pore size, although the enhancement amplitude weakened when the pore size exceeded 3 nm. We further detected the adsorption quantity of the different catalysts at a concentration of 1 mM·NO_3^- (Figure 1d) and found that the adsorption quantity of Ce(IV)-Co_3O_4 was 4.3 times that of Co_3O_4, which showed similar tendencies. These findings indicated that the presence of a Ce−Co dual site in the loose nanoporous structure self-enriched NO_3^-.

Catalytic Performance. The onset potentials of both the NO_3RR and HER were obtained from linear sweep voltammetry (LSV). The more positive onset potential difference was defined as ΔE_{onset}, which is "$E_{onset}(NO_3RR) - E_{onset}(HER)$". Figure 2a illustrates the excellent performance of Ce(IV)-Co_3O_4 in NO_3^- reduction with the positive ΔE_{onset} of 69 mV, of which the onset potential difference was close to that of Pd (55 mV). Note that Pd has previously been reported as the best catalyst in NO_3^- electroreduction.[19,50−53] The Ce(IV)-Co_3O_4 catalyst exhibited performances comparable to Pd for NO_3RR in the presence of a high concentration of NO_3^- (100 mg·L^{-1} NO_3^--N) (Figures S12a and S13a). At a concentration of NO_3^- lower than 100 mg·L^{-1}, Pd and other catalysts were unable to reduce NO_3^- (Figure S12), in which the onset potential differences (ΔE_{onset}) were all negative. For comparison, Ce(IV)-Co_3O_4 exhibited superior NO_3RR (ΔE_{onset}: 47 mV) even at extremely low NO_3 concentrations (1 mg·L^{-1}) (Figures S12h and S13c), suggesting its promising potential for NRA at a low concentration of NO_3^-. The FEs of the above catalytic materials for electroreduction to NH_3 at different NO_3^- concentrations is shown in Figure 2b and Table S3. Obviously, Pd, Co_3O_4, and Ce(IV)-Co_3O_4 all exhibited the best FE at high concentrations of NO_3^- (>1000 mg·L^{-1} NO_3^--N). However, only Ce(IV)-Co_3O_4 still maintained superior FE at low NO_3^- concentrations (10−50 mg·L^{-1} NO_3^--N), while other two cathodes showed a cliff-like drop when the concentration decreased due to the side reaction of hydrogen evolution.

To further investigate the catalytic performance of Ce(IV)-Co_3O_4 for NRA, the surface areas of the catalysts were measured. As shown in Figure S14, Ce(IV)-Co_3O_4/CF (372 cm^2 $_{ECSA}$) had a higher electrochemical surface area (ECSA) than CF (32 cm^2 $_{ECSA}$) and Co_3O_4/CF (292 cm^2 $_{ECSA}$), resulting in a positive impact on the NO_3RR. In addition, the

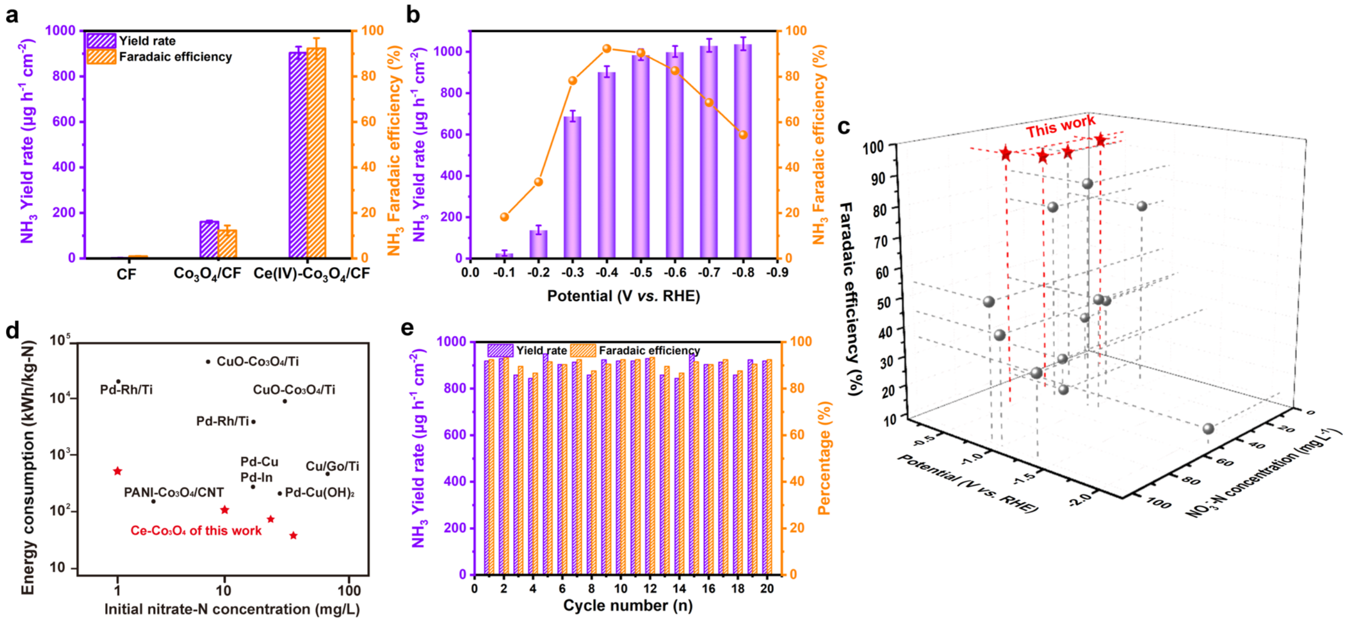

Figure 3. (a) NH_3 yield rate and Faradic efficiency over NO_3^- in (a) different samples and (b) applied potentials. (c) Comparison of the performance of Ce(IV)-Co_3O_4 with other reported catalysts. Red star represents the performance of this work. (d) Energy consumption of the reported electrochemical nitrate reduction studies in a low concentration of NO_3^- via one-step reduction. Starting nitrate concentrations and the corresponding energy consumptions (kWh/kg-N) in the reported electrochemical nitrate reduction studies. (e) Consecutive recycling test at −0.4 V for Ce(IV)-Co_3O_4/CF with 10 mg·L^{-1} NO_3^- for 20 min.

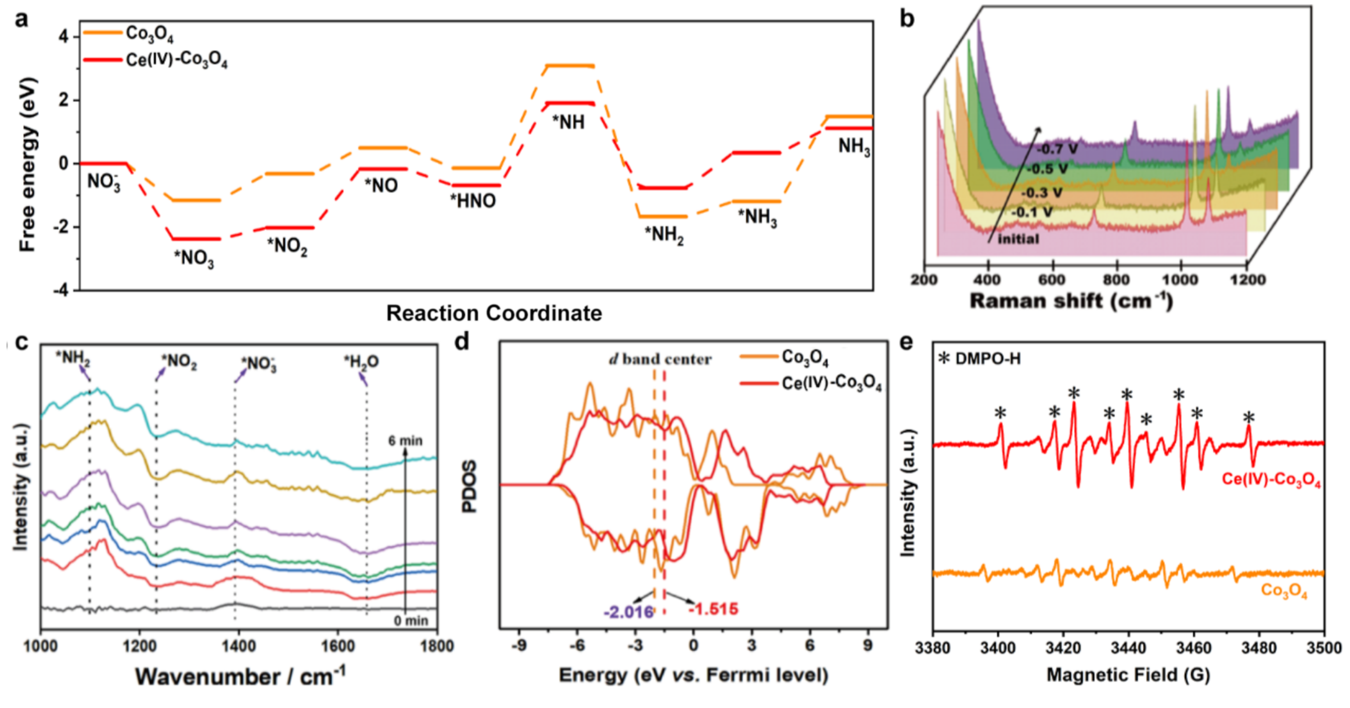

Figure 4. (a) Calculated free energy of the NRA process on Co_3O_4 and Ce(IV)-Co_3O_4. (b) *In situ* Raman spectra at different applied potentials vs RHE. (c) *In situ* FTIR spectra of Ce(IV)-Co_3O_4 under −0.4 V vs RHE with 10 mg·L^{-1} NO_3^-. (d) PDOS of *d*-bands for Co_3O_4 and Ce(IV)-Co_3O_4 and the corresponding *d*-band centers. (e) DMPO spin-trapping ESR spectra of Co_3O_4 and Ce(IV)-Co_3O_4.

Brunauer−Emmett−Teller (BET) surface areas for Co_3O_4 and Ce(IV)−Co_3O_4 were analyzed (Figure S15a). The surface area of Ce(IV)-Co_3O_4 was 8.01 m^2·g^{-1}, which was also 6.2 times higher than that of Co_3O_4 (1.29 m^2·g^{-1}) (Table S4), indicating that the nanoporous structure (10−30 nm) was constructed via the oxyphilic effect of Ce(III) to Ce(IV) (Figure S15b). The cyclic voltammetry (CV) curves with a wider potential range are shown in Figure S16, in which the specific capacity was enhanced with the introduction of Ce.[54] The capacitive contribution of NO_3^- in the double electric layer of Ce(IV)-Co_3O_4 led to the steep characteristic peak at 0.13 V.[55] The Nyquist plots of Ce(IV)-Co_3O_4/CF, Co_3O_4/CF, and CF were obtained via electrochemical impedance spectroscopy (Figure S17), where a smaller arc radius meant lower charge transfer resistance and faster interfacial electron transfer,[56] suggesting the high intrinsic activity of Ce(IV)-Co_3O_4.

Furthermore, the above electrodes were used to test the NRA performance at low concentrations of NO_3^- (10 mg·L^{-1} NO_3^--N and 0.1 M Na_2SO_4) using a three-electrode system, in which the variations of nitrogen compounds were detected by ultraviolet−visible (UV/vis) absorbance spectra (Figure S18). As shown in Figure 3a, Ce(IV)-Co_3O_4/CF showed the best performance of NH_3 yield rate (904 μg·h^{-1}·cm^{-2}) and NH_3 FE (92.3%), better than Co_3O_4/CF (NH_3 FE: 12.3%, NH_3 yield rate: 161 μg·h^{-1}·cm^{-2}) and CF (NH_3 FE: 1.0%, NH_3 yield rate: 2.02 μg·h^{-1}·cm^{-2}). The performance of Ce(IV)-Co_3O_4 was further tested under different applied potentials (Figure 3b). The NH_3 yield rate showed growth as the potential became more negative from −0.1 to −0.8 V vs RHE, while the NH_3 FEs displayed a volcanic trend, which were also much better than those reported by other catalysts (Table S5 and Figure 3c). Thereafter, the catalytic ability of Ce(IV)-Co_3O_4/CF showed a high level in an extremely high concentration of NO_3^- (1000 mg L^{-1} NO_3^--N; Figure S19). Indeed, an energy analysis (Table S6) revealed that the energy consumption of Ce(IV)-Co_3O_4 (149.4 kWh/kg-N) was much lower than that of Co_3O_4 (2180.2 kWh/kg-N) and also outperformed previous reports of using Pd-based and other catalysts (Figure 3d).[37,57−60] Figure S20 shows the variation in NO_3^-, NO_2^-, and NH_3 without the detection of N_2 during the NRA reaction with time. NO_3^- dramatically decreased over 20 min using the Ce(IV)-Co_3O_4/CF electrode and 99.1% of NO_3^- was converted to NH_3, which showed the good NH_3 selectivity. As shown in Figure S21, the FEs of side reactions of H_2 and NO_2^- generation were 6.7% and 0.9%, respectively. After 20 consecutive recycling runs using Ce(IV)-Co_3O_4 (Figure 3e), both the NH_3 yield rate and FEs showed negligible decline, the dissolved Ce and Co ions of Ce(IV)-Co_3O_4 during NO_3RR in electrolyte was negligible (Figure S22), and among the morphology, lamellar structure and valence states were preserved after the electrolysis (Figure S23), confirming the excellent stability and robustness of Ce(IV)-Co_3O_4.

Mechanistic Studies. To gain further insight into the NRA capability of Ce(IV)-Co_3O_4, DFT calculations and experiments were conducted. *In situ* Raman spectra (Figure S24a) showed peaks at approximately 1050 and 980 cm^{-1}, which were assigned to NO_3^- and SO_4^{2-}, respectively, and peaks at 688 and 462 cm^{-1}, which were attributed to the Co−O and O−Ce−O stretching vibration, respectively, indicating the valence states of Co(II) and Ce(IV).[15,61] In Figure S24b, the peaks of Co−O in Co_3O_4 disappeared, indicating that Co(II) was converted into Co^0, while the Co−O and O−Ce−O peaks in Ce(IV)-Co_3O_4 still existed, suggesting the stabilization of the Co intermediate because CeO_2 suppresses the reduction of Co(II) during electrocatalysis.[38] After that, the Gibbs free energies of each step (Figure 4a and Table S7) and the constructed models of Ce(IV)-Co_3O_4 for NRA (Figure S25) were displayed, in which Ce(IV)-Co_3O_4 reduced the reaction energy for the rate-determining step of *HNO to *NH. Finally, the desorption step of NH_3 from *NH_3 on Ce(IV)-Co_3O_4 required lower energy (0.77 eV) owing to the deoxygenation and hydrogenation processes altering the binding sites. Importantly, the plausible intermediate of *NHO or *NOH was compared in the calculation. However, free energy is −0.51 eV for *NHO and 0.21 eV for *NOH (Figure S26), indicating the intermediate of *NHO during NO_3RR. The Raman spectrum was identical when a more negative potential is applied in Ce(IV)-Co_3O_4 (Figure 4b), indicating that HER was not likely to occur. As shown in electrochemical in situ attenuated total reflectance (ATR)-FTIR spectroscopy (Figure 4c), the asymmetric stretching vibration of NO_3^- appeared at 1392 cm^{-1} and the downward band at 1638 cm^{-1}, indicating the enrichment of NO_3^- and the generation of H* for NO_3^- deoxygenation.[62] The projected density of states (PDOS) associated with the electronic structure was calculated (Figure 4d), and the corresponding *d*-band centers of Co_3O_4 and Ce(IV)-Co_3O_4 were −2.016 and −1.515 eV vs the Fermi level. The right shift of the PDOS with the distribution of *d*-band electrons relatively closer to the Fermi level for Ce(IV)-Co_3O_4 indicated the adsorption for the critical intermediates of *NO_2, *NO, *HNO, *NH, and *NH_2 by the NRA reaction (Figure S27). Furthermore, the formation of H* was detected during the NRA reaction, in which 5,5-dimethyl-1-pyrroline-N-oxide (DMPO) was used as the quenching reagent. The signals of the nine characteristic peaks of DMPO-H (1:1:2:1:2:1:2:1:1:1) for Ce(IV)-Co_3O_4 were much stronger and clearer (Figure 4e), as more O_{vs} in Ce(IV)-Co_3O_4 strengthened the activation of H^+ into H*. Note that in the presence of NO_3^-, the DMPO-H peaks of Ce(IV)-Co_3O_4 disappeared (Figure S28), suggesting that H* was consumed for NRA reaction. The DFT calculation revealed that the required energy for Ce(IV)-Co_3O_4 (0.86 eV) to form H* was much lower than that of Co_3O_4 (1.51 eV), also confirming the positive effect of the O_{vs} on H* generation (Figure S29). The quenching experiments were applied to deeply identify the H* role, in which *tert*-butyl alcohol (TBA) was used as the specific H* quenching agent.[10] The conversion of NO_3^- continuously decreased as the concentration of TBA was increased from 0 to 10 mM (Figure S30a,b). Moreover, Figure S31 intuitively shows the FEs at different Ce contents. Of these, excessive Ce (IV) entering Co_3O_4 significantly altered the distribution of O around Co to change the synergistic reactive performance of self-enrichment and O_{vs} amplification. Excessive Ce and O_{vs} could alter the structure of the nanosheets to affect the utilization of H* and reduced the NH_3 FE, indicating the intrinsic activity of suitable equilibrium of NO_3^- self-enrichment and H* production. Based on all of the theoretical calculations and experiments, the introduction of Ce ions were allowed to enrich NO_3^-, modulate the *d*-band center, and enhance the generation of H*, thus leading to the highly selective reduction of low concentrations of NO_3^- to NH_3.

■ ENVIRONMENTAL APPLICATION

The elimination of low concentrations of NO_3^- is essential, and converting it into higher-value NH_3 is a very attractive approach to validate a widely aqueous pollutant to valuable chemical feedstock. However, with the progress of electroreduction, H* easily formed the H_2 overflow owing to the poor accessibility of NO_3^- on the cathodic surface at low concentrations of NO_3^-. In this work, the designed Ce(IV)-Co_3O_4 was fabricated by inserting CeO_2 into Co_3O_4, featuring a bifunctional role: (1) the strong self-enrichment of NO_3^- via the efficient adsorption of the Ce−Co dual site and (2) the generation of O_v near the Ce−Co dual site to effectively generate H*. Hence, the Ce(IV)-Co_3O_4 with excellent stability allowed to convert NO_3^- into NH_3 with a high NH_3 FE and a low energy consumption at a wide NO_3^- concentrations range, including low or even ultralow concentrations (10−1000 mg·L^{-1} NO_3^--N), substantially exceeding previously reported catalysts including Pd-based catalysts. Even the electrochemical reduction of a high concentration of NO_3^- continuously diluted with NO_3^- still maintained the electrocatalytic NRA, which expanded the application of the electrochemical NO_3^- treatment. Thereafter, actual water from different sources, including industrial wastewater, post-treated wastewater, and natural surface water, were collected to explore the application of the Ce(IV)-Co_3O_4 cathode. As shown in Table S8, NO_3^-, in all kinds of actual water bodies with a wide concentration range (10−1000 mg·L^{-1} NO_3^--N), was effectively eliminated and further converted to NH_3. Furthermore, consecutive recycling tests were used to evaluate the longevity of Ce(IV)-Co_3O_4 in actual surface water treatment. After consecutive recycling runs, the performance of NO_3^- elimination and NH_3 generation have no significant variation (Figure S32). As the reduction of NO_3^- consumed H^+, the pH value increases during the reaction (Figure S33). In addition, different kinds of anions were added into the simulated solution to confirm the NO_3RR performance of Ce(IV)-Co_3O_4; obviously, different anions had almost no impact on the NO_3^- reduction of Ce(IV)-Co_3O_4 electrode (Figure S34). The costs compared to other catalysts were also investigated and are listed in Table S9, with Ce(IV)-Co_3O_4 showing the lowest cost of NH_3 production in all kinds of real wastewater treatments. Hence, our work provides a facile synthesis method for efficient NRA reactions at a wide NO_3^- concentration range and can facilitate an efficient strategy for treating wastewater with low concentrations of NO_3^-.

■ ASSOCIATED CONTENT

Supporting Information

The Supporting Information is available free of charge at https://pubs.acs.org/doi/10.1021/acs.est.4c06263.

> Detailed experimental studies; simulated methods; computational methods; additional SEM and TEM images; XRD results; XPS spectra; electrochemical measurements; and quantification of products and DFT data (PDF)

■ AUTHOR INFORMATION

Corresponding Authors

Jing Bai − *School of Environmental Science and Engineering, Key Laboratory of Thin Film and Microfabrication Technology (Ministry of Education), Shanghai Jiao Tong University, Shanghai 200240, China;* orcid.org/0000-0001-6957-190X; Email: bai_jing@sjtu.edu.cn

Baoxue Zhou − *School of Environmental Science and Engineering, Key Laboratory of Thin Film and Microfabrication Technology (Ministry of Education), Shanghai Jiao Tong University, Shanghai 200240, China; Shanghai Institute of Pollution Control and Ecological Security, Shanghai 200092, China;* orcid.org/0000-0001-9691-3119; Email: zhoubaoxue@sjtu.edu.cn

Gengfeng Zheng − *Laboratory of Advanced Materials, Department of Chemistry, Fudan University, Shanghai 200438, China;* orcid.org/0000-0002-1803-6955; Email: gfzheng@fudan.edu.cn

Authors

Changhui Zhou − *School of Environmental Science and Engineering, Key Laboratory of Thin Film and Microfabrication Technology (Ministry of Education), Shanghai Jiao Tong University, Shanghai 200240, China*

Yan Zhang − *School of Environmental Science and Engineering, Key Laboratory of Thin Film and Microfabrication Technology (Ministry of Education), Shanghai Jiao Tong University, Shanghai 200240, China;* orcid.org/0000-0003-0214-3147

Chaoyue Xie − *School of Environmental Science and Engineering, Key Laboratory of Thin Film and Microfabrication Technology (Ministry of Education), Shanghai Jiao Tong University, Shanghai 200240, China*

Jinhua Li − *School of Environmental Science and Engineering, Key Laboratory of Thin Film and Microfabrication Technology (Ministry of Education), Shanghai Jiao Tong University, Shanghai 200240, China*

Haichuan Zhang − *Hefei National Laboratory for Physical Science at the Microscale, University of Science and Technology of China, Hefei, Anhui 230026, China*

Hong Zhu − *University of Michigan-Shanghai Jiao Tong University Joint Institute, Shanghai Jiao Tong University, Shanghai 200240, China;* orcid.org/0000-0001-7919-5661

Mingce Long − *School of Environmental Science and Engineering, Key Laboratory of Thin Film and Microfabrication Technology (Ministry of Education), Shanghai Jiao Tong University, Shanghai 200240, China;* orcid.org/0000-0002-5168-8330

Complete contact information is available at: https://pubs.acs.org/10.1021/acs.est.4c06263

Notes

The authors declare no competing financial interest.

■ ACKNOWLEDGMENTS

The authors acknowledge the National Natural Science Foundation of China (Nos. 22076121, 22206123, U23A20552, 22178220, and 22025502), the China Postdoctoral Science Foundation (2022M722081 and 2021M692064), the Fundamental Research Funds for the Central Universities, and the AEMD center (SJTU) and instrumental Analysis Center (SJTU-SESE) for support.

■ REFERENCES

(1) Yu, C.; Huang, X.; Chen, H.; Godfray, H. C. J.; Wright, J. S.; Hall, J. W.; Gong, P.; Ni, S.; Qiao, S.; Huang, G.; Xiao, Y.; Zhang, J.; Feng, Z.; Ju, X.; Ciais, P.; Stenseth, N. C.; Hessen, D. O.; Sun, Z.; Yu, L.; Cai, W.; Fu, H.; Huang, X.; Zhang, C.; Liu, H.; Taylor, J. Managing nitrogen to restore water quality in China. *Nature* **2019**, *567* (7749), 516−520.

(2) Luo, Y.; Xie, K.; Ou, P.; Lavallais, C.; Peng, T.; Chen, Z.; Zhang, Z.; Wang, N.; Li, X.-Y.; Grigioni, I.; Liu, B.; Sinton, D.; Dunn, J. B.; Sargent, E. H. Selective electrochemical synthesis of urea from nitrate and CO_2 via relay catalysis on hybrid catalysts. *Nat. Catal* **2023**, *6* (10), 939−948.

(3) Sun, J.; Garg, S.; Waite, T. D. A Novel Integrated Flow-Electrode Capacitive Deionization and Flow Cathode System for Nitrate Removal and Ammonia Generation from Simulated Groundwater. *Environ. Sci. Technol.* **2023**, *57* (39), 14726−14736.

(4) Liu, C.; Wang, H.; Ma, Q.; Ma, J.; Wang, Z.; Liang, L.; Xu, W.; Zhang, G.; Zhang, X.; Wang, T.; He, H. Efficient Conversion of NO to NO_2 on SO_2-Aged MgO under Atmospheric Conditions. *Environ. Sci. Technol.* **2020**, *54* (19), 11848−11856.

(5) Su, J. F.; Kuan, W.-F.; Liu, H.; Huang, C. P. Mode of electrochemical deposition on the structure and morphology of bimetallic electrodes and its effect on nitrate reduction toward nitrogen selectivity. *Appl. Catal., B* **2019**, *257*, No. 117909.

(6) Fan, Y.; Wang, X.; Butler, C.; Kankam, A.; Belgada, A.; Simon, J.; Gao, Y.; Chen, E.; Winter, L. R. Highly efficient metal-free nitrate reduction enabled by electrified membrane filtration. *Nat. Water* **2024**, *2*, 684−696.

(7) Zhang, K.; Cao, A.; Wandall, L. H.; Vernieres, J.; Kibsgaard, J.; Nørskov, J. K.; Chorkendorff, I. Spin-mediated promotion of Co catalysts for ammonia synthesis. *Science* **2024**, *383* (6689), 1357−1363.

(8) Yin, H.; Chen, Z.; Peng, Y.; Xiong, S.; Li, Y.; Yamashita, H.; Li, J. Dual Active Centers Bridged by Oxygen Vacancies of Ruthenium Single-Atom Hybrids Supported on Molybdenum Oxide for Photocatalytic Ammonia Synthesis. *Angew. Chem., Int. Ed.* **2022**, *61* (14), No. e202114242.

(9) Liu, Y.; Wei, J.; Yang, Z.; Zheng, L.; Zhao, J.; Song, Z.; Zhou, Y.; Cheng, J.; Meng, J.; Geng, Z.; Zeng, J. Efficient tandem electroreduction of nitrate into ammonia through coupling Cu single atoms with adjacent Co_3O_4. *Nat. Commun.* **2024**, *15* (1), No. 3619.

(10) Fan, K.; Xie, W.; Li, J.; Sun, Y.; Xu, P.; Tang, Y.; Li, Z.; Shao, M. Active hydrogen boosts electrochemical nitrate reduction to ammonia. *Nat. Commun.* **2022**, *13* (1), No. 7958.

(11) Wu, Z. Y.; Karamad, M.; Yong, X.; Huang, Q.; Cullen, D. A.; Zhu, P.; Xia, C.; Xiao, Q.; Shakouri, M.; Chen, F. Y.; Kim, J. Y. T.; Xia, Y.; Heck, K.; Hu, Y.; Wong, M. S.; Li, Q.; Gates, I.; Siahrostami, S.; Wang, H. Electrochemical ammonia synthesis via nitrate reduction on Fe single atom catalyst. *Nat. Commun.* **2021**, *12* (1), No. 2870.

(12) Chen, G.-F.; Yuan, Y.; Jiang, H.; Ren, S.-Y.; Ding, L.-X.; Ma, L.; Wu, T.; Lu, J.; Wang, H. Electrochemical reduction of nitrate to ammonia via direct eight-electron transfer using a copper−molecular solid catalyst. *Nat. Energy* **2020**, *5* (8), 605−613.

(13) Feng, A.; Hu, Y.; Yang, X.; Lin, H.; Wang, Q.; Xu, J.; Liu, A.; Wu, G.; Li, Q. ZnO Nanowire Arrays Decorated with Cu Nanoparticles for High-Efficiency Nitrate to Ammonia Conversion. *ACS Catal.* **2024**, *14* (8), 5911−5923.

(14) Huang, Y.; He, C.; Cheng, C.; Han, S.; He, M.; Wang, Y.; Meng, N.; Zhang, B.; Lu, Q.; Yu, Y. Pulsed electroreduction of low-concentration nitrate to ammonia. *Nat. Commun.* **2023**, *14* (1), No. 7368.

(15) Han, S.; Li, H.; Li, T.; Chen, F.; Yang, R.; Yu, Y.; Zhang, B. Ultralow overpotential nitrate reduction to ammonia via a three-step relay mechanism. *Nat. Catal* **2023**, *6*, 402−414.

(16) Ni, J.; Wen, Y.; Pan, D.; Bai, J.; Zhou, B.; Zhao, S.; Wang, Z.; Liu, Y.; Zeng, Q. Light-driven simultaneous water purification and green energy production by photocatalytic fuel cell: A comprehensive review on current status, challenges, and perspectives. *Chem. Eng. J.* **2023**, *473*, No. 145162.

(17) Zhang, W.; Yao, Y.; Chen, Z.; Zhao, S.; Guo, F.; Zhang, L. Fluorine Modification Promoted Water Dissociation into Atomic Hydrogen on a Copper Electrode for Efficient Neutral Nitrate Reduction and Ammonia Recovery. *Environ. Sci. Technol.* **2024**, *58* (16), 7208−7216.

(18) Bu, Y.; Yu, W.; Yang, Q.; Zhang, W.; Sun, Q.; Wu, W.; Cui, P.; Wang, C.; Gao, G. Membraneless Electrochemical Synthesis Strategy toward Nitrate-to-Ammonia Conversion. *Environ. Sci. Technol.* **2024**, *58* (28), 12708−12718.

(19) Liang, X.; Zhu, H.; Yang, X.; Xue, S.; Liang, Z.; Ren, X.; Liu, A.; Wu, G. Recent Advances in Designing Efficient Electrocatalysts for Electrochemical Nitrate Reduction to Ammonia. *Small Struct.* **2022**, *4* (6), No. 2200202.

(20) Wang, Y.; Zhou, W.; Jia, R.; Yu, Y.; Zhang, B. Unveiling the Activity Origin of a Copper-based Electrocatalyst for Selective Nitrate Reduction to Ammonia. *Angew. Chem., Int. Ed.* **2020**, *59* (13), 5350−5354.

(21) Chen, F.-Y.; Wu, Z.-Y.; Gupta, S.; Rivera, D. J.; Lambeets, S. V.; Pecaut, S.; Kim, J. Y. T.; Zhu, P.; Finfrock, Y. Z.; Meira, D. M.; King, G.; Gao, G.; Xu, W.; Cullen, D. A.; Zhou, H.; Han, Y.; Perea, D. E.; Muhich, C. L.; Wang, H. Efficient conversion of low-concentration nitrate sources into ammonia on a Ru-dispersed Cu nanowire electrocatalyst. *Nat. Nanotechnol.* **2022**, *17*, 759−767.

(22) Deng, X.; Yang, Y.; Wang, L.; Fu, X. Z.; Luo, J. L. Metallic Co Nanoarray Catalyzes Selective NH_3 Production from Electrochemical Nitrate Reduction at Current Densities Exceeding 2 A cm^{-2}. *Adv. Sci.* **2021**, *8* (7), No. 2004523.

(23) Guo, Y.; Zhang, R.; Zhang, S.; Zhao, Y.; Yang, Q.; Huang, Z.; Dong, B.; Zhi, C. Pd doping-weakened intermediate adsorption to promote electrocatalytic nitrate reduction on TiO_2 nanoarrays for ammonia production and energy supply with zinc−nitrate batteries. *Energy Environ. Sci.* **2021**, *14* (7), 3938−3944.

(24) Li, J.; Zhan, G.; Yang, J.; Quan, F.; Mao, C.; Liu, Y.; Wang, B.; Lei, F.; Li, L.; Chan, A. W. M.; Xu, L.; Shi, Y.; Du, Y.; Hao, W.; Wong, P. K.; Wang, J.; Dou, S. X.; Zhang, L.; Yu, J. C. Efficient Ammonia Electrosynthesis from Nitrate on Strained Ruthenium Nanoclusters. *J. Am. Chem. Soc.* **2020**, *142* (15), 7036−7046.

(25) Wang, Y.; Xu, A.; Wang, Z.; Huang, L.; Li, J.; Li, F.; Wicks, J.; Luo, M.; Nam, D. H.; Tan, C. S.; Ding, Y.; Wu, J.; Lum, Y.; Dinh, C. T.; Sinton, D.; Zheng, G.; Sargent, E. H. Enhanced Nitrate-to-Ammonia Activity on Copper-Nickel Alloys via Tuning of Intermediate Adsorption. *J. Am. Chem. Soc.* **2020**, *142* (12), 5702−5708.

(26) Zhang, S.; Li, M.; Li, J.; Song, Q.; Liu, X. High-ammonia selective metal-organic framework-derived Co-doped Fe/Fe_2O_3 catalysts for electrochemical nitrate reduction. *Proc. Natl. Acad. Sci. U.S.A.* **2022**, *119* (6), No. e2115504119.

(27) Wang, Y.; Wang, C.; Li, M.; Yu, Y.; Zhang, B. Nitrate electroreduction: mechanism insight, in situ characterization, performance evaluation, and challenges. *Chem. Soc. Rev.* **2021**, *50* (12), 6720−6733.

(28) Sun, S.; Dai, C.; Zhao, P.; Xi, S.; Ren, Y.; Tan, H. R.; Lim, P. C.; Lin, M.; Diao, C.; Zhang, D.; Wu, C.; Yu, A.; Koh, J. C. J.; Lieu, W. Y.; Seng, D. H. L.; Sun, L.; Li, Y.; Tan, T. L.; Zhang, J.; Xu, Z. J.; Seh, Z. W. Spin-related Cu-Co pair to increase electrochemical ammonia generation on high-entropy oxides. *Nat. Commun.* **2024**, *15* (1), No. 260.

(29) Sun, W. J.; Ji, H. Q.; Li, L. X.; Zhang, H. Y.; Wang, Z. K.; He, J. H.; Lu, J. M. Built-in Electric Field Triggered Interfacial Accumulation Effect for Efficient Nitrate Removal at Ultra-Low Concentration and Electroreduction to Ammonia. *Angew. Chem., Int. Ed.* **2021**, *60* (42), 22933−22939.

(30) Choi, C.; Wang, X.; Kwon, S.; Hart, J. L.; Rooney, C. L.; Harmon, N. J.; Sam, Q. P.; Cha, J. J.; Goddard, W. A., 3rd; Elimelech, M.; Wang, H. Efficient electrocatalytic valorization of chlorinated organic water pollutant to ethylene. *Nat. Nanotechnol.* **2023**, *18* (2), 160−167.

(31) Zhou, J.; Zhu, Y.; Wen, K.; Pan, F.; Ma, H.; Niu, J.; Wang, C.; Zhao, J. Efficient and Selective Electrochemical Nitrate Reduction to N_2 Using a Flow-Through Zero-Gap Electrochemical Reactor with a Reconstructed $Cu(OH)_2$ Cathode: Insights into the Importance of Inter-Electrode Distance. *Environ. Sci. Technol.* **2024**, *58* (10), 4824−4836.

(32) Kurban, M.; Zhang, Y.; Wang, Y.; Su, Z.; Zhou, T.; Zhou, C.; Xie, C.; Li, L.; Li, J.; Bai, J.; Zhou, B. Chlorine oxide radical: An emerging free radical for denitrification and pollutant degradation. *J. Environ. Chem. Eng.* **2024**, *12* (3), No. 112630.

(33) van Langevelde, P. H.; Katsounaros, I.; Koper, M. T. M. Electrocatalytic Nitrate Reduction for Sustainable Ammonia Production. *Joule* **2021**, *5*, 290−294.

(34) Liu, H.; Park, J.; Chen, Y.; Qiu, Y.; Cheng, Y.; Srivastava, K.; Gu, S.; Shanks, B. H.; Roling, L. T.; Li, W. Electrocatalytic Nitrate Reduction on Oxide-Derived Silver with Tunable Selectivity to Nitrite and Ammonia. *ACS Catal.* **2021**, *11* (14), 8431−8442.

(35) Zhou, C.; Bai, J.; Zhang, Y.; Li, J.; Li, Z.; Jiang, P.; Fang, F.; Zhou, M.; Mei, X.; Zhou, B. Novel 3D Pd-$Cu(OH)_2$/CF cathode for rapid reduction of nitrate-N and simultaneous total nitrogen removal from wastewater. *J. Hazard. Mater.* **2021**, *401*, No. 123232.

(36) Ward, M. H.; Brender, J. D. Drinking Water Nitrate and Human Health. In *Encyclopedia of Environmental Health*, 2nd ed.; Nriagu, J., Ed.; Elsevier: Oxford, 2019; pp 173−186.

(37) Kim, K.; Zagalskaya, A.; Ng, J. L.; Hong, J.; Alexandrov, V.; Pham, T. A.; Su, X. Coupling nitrate capture with ammonia production through bifunctional redox-electrodes. *Nat. Commun.* **2023**, *14* (1), No. 823.

(38) Huang, J.; Sheng, H.; Ross, R. D.; Han, J.; Wang, X.; Song, B.; Jin, S. Modifying redox properties and local bonding of Co3O4 by CeO2 enhances oxygen evolution catalysis in acid. *Nat. Commun.* **2021**, *12* (1), No. 3036.

(39) Song, C.; Zhan, Q.; Liu, F.; Wang, C.; Li, H.; Wang, X.; Guo, X.; Cheng, Y.; Sun, W.; Wang, L.; Qian, J.; Pan, B. Overturned Loading of Inert CeO_2 to Active Co_3O_4 for Unusually Improved Catalytic Activity in Fenton-Like Reactions. *Angew. Chem., Int. Ed.* **2022**, *61* (16), No. e202200406.

(40) Jian, Y.; Tian, M.; He, C.; Xiong, J.; Jiang, Z.; Jin, H.; Zheng, L.; Albilali, R.; Shi, J.-W. Efficient propane low-temperature destruction by Co_3O_4 crystal facets engineering: Unveiling the decisive role of lattice and oxygen defects and surface acid-base pairs. *Appl. Catal., B* **2021**, *283*, No. 119657.

(41) Dubey, K.; Dubey, S.; Sahu, V.; Modi, A.; Bamne, J.; Haque, F. Z.; Gaur, N. K. Defects and oxygen vacancies modified properties of transition metal doped Ce0.95 × 0.05O2 (X = Fe, Co, Ni) nanoparticles. *Mater. Sci. Eng.: B* **2023**, *288*, No. 116154, DOI: 10.1016/j.mseb.2022.116154.

(42) Rokicińska, A.; Natkański, P.; Dudek, B.; Drozdek, M.; Lityńska-Dobrzyńska, L.; Kuśtrowski, P. Co_3O_4-pillared montmorillonite catalysts synthesized by hydrogel-assisted route for total oxidation of toluene. *Appl. Catal., B* **2016**, *195*, 59−68.

(43) Liu, G.; Xie, C.; Zhang, Y.; Du, Y.; Wang, J.; Lin, J.; Bai, J.; Li, J.; Zhou, C.; Zhou, T.; Zhou, B. Synergistic etching of nickel foam by Fe^{3+} and Cl^- ions to synthesize nickel-iron-layered double hydroxide nanolayers with abundant oxygen vacancies for superior urea oxidation. *J. Colloid Interface Sci.* **2024**, *668*, 375−384.

(44) Liu, Y.; Ma, C.; Zhang, Q.; Wang, W.; Pan, P.; Gu, L.; Xu, D.; Bao, J.; Dai, Z. 2D Electron Gas and Oxygen Vacancy Induced High Oxygen Evolution Performances for Advanced Co_3O_4 /CeO_2 Nanohybrids. *Adv. Mater.* **2019**, *31* (21), No. e1900062.

(45) Liu, Xiangwen.; Z, K.; Wang, Lei.; Wang, Baoyi.; Li, Yadong. Oxygen Vacancy Clusters Promoting Reducibility and Activity of Ceria Nanorods. *J. Am. Chem. Soc.* **2009**, *131*, 3140−3141.

(46) Jiang, J.; Li, L. Synthesis of sphere-like Co_3O_4 nanocrystals via a simple polyol route. *Mater. Lett.* **2007**, *61* (27), 4894−4896.

(47) Deng, Z.; Ma, C.; Li, Z.; Luo, Y.; Zhang, L.; Sun, S.; Liu, Q.; Du, J.; Lu, Q.; Zheng, B.; Sun, X. High-Efficiency Electrochemical Nitrate Reduction to Ammonia on a Co_3O_4 Nanoarray Catalyst with Cobalt Vacancies. *ACS Appl. Mater. Interfaces* **2022**, *14* (41), 46595−46602.

(48) Chang, Z.; Meng, G.; Chen, Y.; Chen, C.; Han, S.; Wu, P.; Zhu, L.; Tian, H.; Kong, F.; Wang, M.; Cui, X.; Shi, J. Dual-Site W-O-CoP Catalysts for Active and Selective Nitrate Conversion to Ammonia in a Broad Concentration Window. *Adv. Mater.* **2023**, *35* (32), No. e2304508.

(49) Huo, Z. Y.; Winter, L. R.; Wang, X. X.; Du, Y.; Wu, Y. H.; Hubner, U.; Hu, H. Y.; Elimelech, M. Synergistic Nanowire-Enhanced Electroporation and Electrochlorination for Highly Efficient Water Disinfection. *Environ. Sci. Technol.* **2022**, *56* (15), 10925−10934.

(50) Sun, L.; Liu, B. Mesoporous PdN Alloy Nanocubes for Efficient Electrochemical Nitrate Reduction to Ammonia. *Adv. Mater.* **2023**, *35* (1), No. e2207305.

(51) Sun, J.; Yang, H.; Gao, W.; Cao, T.; Zhao, G. Diatomic Pd-Cu Metal-Phosphorus Sites for Complete N identical withN Bond Formation in Photoelectrochemical Nitrate Reduction. *Angew. Chem., Int. Ed.* **2022**, *61* (45), No. e202211373.

(52) Trawczyński, J.; Gheek, P.; Okal, J.; Zawadzki, M.; Gomez, M. J. I. Reduction of nitrate on active carbon supported Pd-Cu catalysts. *Appl. Catal., A* **2011**, *409−410*, 39−47.

(53) Sun, C.; Li, F.; An, H.; Li, Z.; Bond, A. M.; Zhang, J. Facile electrochemical co-deposition of metal (Cu, Pd, Pt, Rh) nanoparticles on reduced graphene oxide for electrocatalytic reduction of nitrate/nitrite. *Electrochim. Acta* **2018**, *269*, 733−741.

(54) Guo, X.; Wang, C.; Wang, W.; Zhou, Q.; Xu, W.; Zhang, P.; Wei, S.; Cao, Y.; Zhu, K.; Liu, Z.; Yang, X.; Wang, Y.; Wu, X.; Song, L.; Chen, S.; Liu, X. Vacancy manipulating of molybdenum carbide MXenes to enhance Faraday reaction for high performance lithium-ion batteries. *Nano Res. Energy* **2022**, *1*, No. 9120026.

(55) El-Deab, M. S. Electrochemical reduction of nitrate to ammonia at modified gold electrodes. *Electrochim. Acta* **2004**, *49* (9−10), 1639−1645.

(56) Zhou, C.; Li, J.; Wang, J.; Xie, C.; Zhang, Y.; Li, L.; Zhou, T.; Bai, J.; Zhu, H.; Zhou, B. Efficient H_2 production and TN removal for urine disposal using a novel photoelectrocatalytic system of Co_3O_4/$BiVO_4$ - $MoNiCuO_x$/Cu. *Appl. Catal., B* **2023**, *324*, No. 12229.

(57) Cheng, H.; Scott, K.; Christensen, P. A. Paired electrolysis in a solid polymer electrolyte reactor—Simultaneously reduction of nitrate and oxidation of ammonia. *Chem. Eng. J.* **2005**, *108* (3), 257−268.

(58) Yang, M.; Wang, J.; Shuang, C.; Li, A. The improvement on total nitrogen removal in nitrate reduction by using a prepared CuO−Co_3O_4/Ti cathode. *Chemosphere* **2020**, *255*, No. 126970.

(59) Gayen, P.; Spataro, J.; Avasarala, S.; Ali, A.-M.; Cerrato, J. M.; Chaplin, B. P. Electrocatalytic Reduction of Nitrate Using Magnéli Phase TiO_2 Reactive Electrochemical Membranes Doped with Pd-Based Catalysts. *Environ. Sci. Technol.* **2018**, *52* (16), 9370−9379.

(60) Wang, J.; Wang, S.; Zhang, Z.; Wang, C. Preparation of Cu/GO/Ti electrode by electrodeposition and its enhanced electrochemical reduction for aqueous nitrate. *J. Environ. Manage* **2020**, *276*, No. 111357.

(61) Jiang, F.; Wang, S.; Liu, B.; Liu, J.; Wang, L.; Xiao, Y.; Xu, Y.; Liu, X. Insights into the Influence of CeO_2 Crystal Facet on CO_2 Hydrogenation to Methanol over Pd/CeO_2 Catalysts. *ACS Catal.* **2020**, *10* (19), 11493−11509.

(62) Fang, J. Y.; Zheng, Q. Z.; Lou, Y. Y.; Zhao, K. M.; Hu, S. N.; Li, G.; Akdim, O.; Huang, X. Y.; Sun, S. G. Ampere-level current density ammonia electrochemical synthesis using CuCo nanosheets simulating nitrite reductase bifunctional nature. *Nat. Commun.* **2022**, *13* (1), No. 7899.